Composites Science and Technology 186 (2020) 107922

Contents lists available at ScienceDirect

Composites Science and Technology

journal homepage: www.elsevier.com/locate/compscitech

Predictive multiscale modeling for Unidirectional Carbon Fiber Reinforced Polymers

Jiaying Gao [a], Modesar Shakoor [a], Gino Domel [b], Matthias Merzkirch [c], Guowei Zhou [d], Danielle Zeng [d], Xuming Su [d], Wing Kam Liu [a,*]

[a] *Department of Mechanical Engineering, Northwestern University, Evanston, IL 60208, United States*
[b] *Department of Mechanical Engineering, University of Notre Dame, Notre Dame, IN 46556, United States*
[c] *Guest Researcher at National Institute of Standards and Technology, 100 Bureau Dr, Gaithersburg, MD 20899, United States*
[d] *Research and Advanced Engineering, Ford Motor Company, Dearborn, MI 48121, United States*

ARTICLE INFO

Keywords:
Integrated Computational Material and Engineering (ICME)
Data-driven
Multiscale modeling
Structural performance prediction
Carbon fiber reinforced polymers

ABSTRACT

This paper presents a predictive multiscale modeling scheme for Unidirectional (UD) Carbon Fiber Reinforced Polymers (CFRP). A bottom-up modeling procedure is discussed for predicting the performance of UD structures. UD material responses are computed from high fidelity Representative Volume Elements (RVEs). A data-driven Reduced Order Modeling approach compresses RVEs into Reduced Order Models so material responses can be computed in a concurrent fashion along with the structural level simulation. The approach presented in this paper is validated against experimental data and is believed to provide design guidance for future fiber reinforced polymers development.

1. Introduction

In modern engineering applications, composite materials are receiving growing attention for their extraordinary lightweight and strength. To understand the mechanical performance of various CFRP designs, physical tests are necessary. With computational power continually growing, it is now possible to utilize the Integrated Computational Material Engineering (ICME) approach to virtually evaluate the performance of composite designs and provide design guidance for composite materials. The ICME approach directly integrates microstructure information into property and performance prediction [1,2]. In the ICME process, the intrinsic relationship between material microstructure and mechanical performance can be captured by a multiscale model which links microstructure to macroscale performance. In this manuscript, a bottom-up ICME modeling framework for UD CFRP is introduced. The framework incorporates a two-stage Reduced Order Modeling (ROM) technique that enables rapid computation of UD microstructure nonlinear responses during UD CFRP structures simulation. The bottom-up multiscale modeling workflow for UD CFRP is explained in Fig. 1.

There has been considerable effort during the past decades in incorporating microstructure information to the macroscale model for performance prediction. For example, one can model all microstructure details into a single model, but this computation is expensive due to the fine mesh required [3]. By deploying multiscale modeling techniques, the macroscale responses are predicted with physical microscale information [4–7]. A hierarchical multiscale modeling approach as demonstrated in [8,9] by the Multiresolution Continuum Theory is one of them. In the Multiresolution Continuum Theory, the microstructure information is implemented into the macroscale constitutive law to construct a hierarchical multiscale model, which captures microstructural effects, such as the effect of inclusion size. Although this hierarchical multiscale modeling method preserves certain microstructure information, it does not provide explicit microstructure evolution.

To capture microstructure responses, concurrent homogenization can be deployed. A detailed review of this topic is summarized by Geers et al. in [10]. One of the concurrent homogenization schemes is the Finite Element square (FE^2) approach. In the FE^2 approach, the macroscale geometry is discretized with a Finite Element (FE) mesh. Material responses at all integration points are computed by solving RVEs that are discretized with FE meshes. The FE^2 approach solves two sets of FE meshes in a concurrent fashion, which results in high computational cost.

To improve computational efficiency, various ROM approaches were developed, such as Transformation Field Analysis [11], Nonuniform Transformation Field Analysis [12,13] and Proper Orthogonal Decomposition [14,15]. A newly proposed data-driven two-stage ROM approach, namely Self-consistent Clustering Analysis (SCA) [16], creates ROMs from high fidelity voxel mesh RVEs and simulates RVEs'

---

[*] Corresponding author.
E-mail address: w-liu@northwestern.edu (W.K. Liu).

https://doi.org/10.1016/j.compscitech.2019.107922
Received 15 April 2019; Received in revised form 9 November 2019; Accepted 17 November 2019
Available online 20 November 2019
0266-3538/© 2019 Elsevier Ltd. All rights reserved.

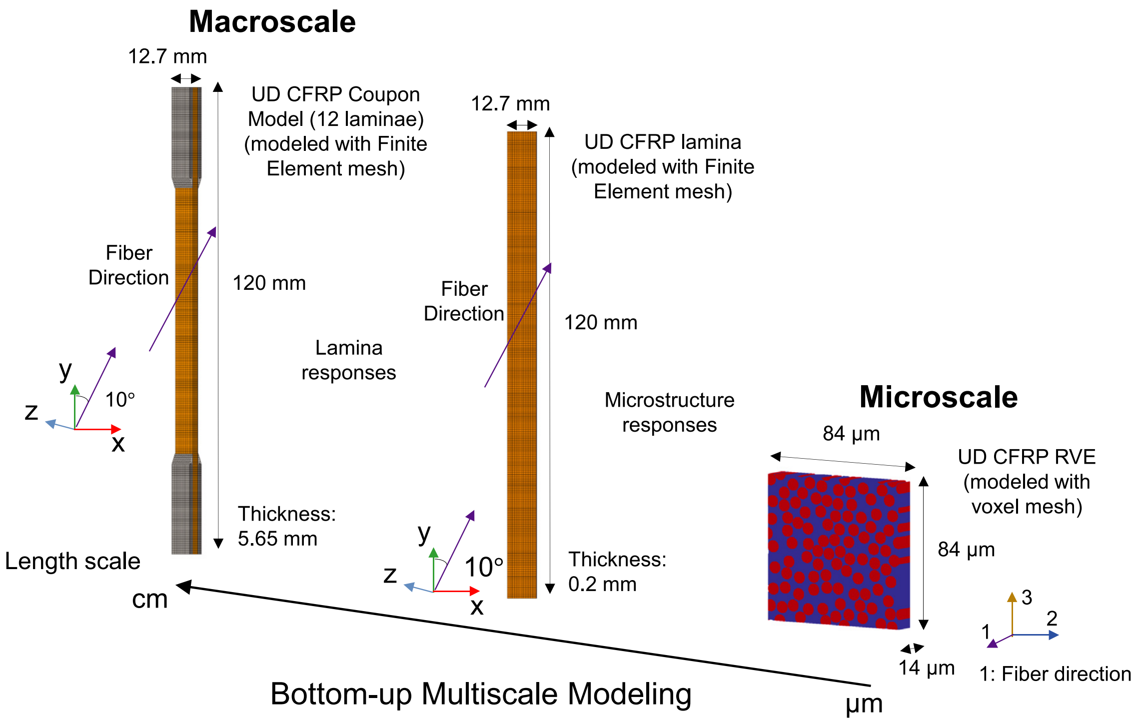

Fig. 1. ICME framework illustration. This figure illustrates the length scale span in the modeling process. The UD CFRP microstructure at micron scale, characterization by UD RVE, provides microstructure information for UD lamina and UD coupon at millimeter scale. Accurate UD structure responses are predicted using physical RVEs. From the microscale (the UD microstructure) to the macroscale (the UD Coupon FE mesh), the UD Coupon is modeled in a bottom up fashion. This framework can be extended to 3-scale composites, including UD, woven and woven laminate structures.

elasto-plastic behaviors with an effective RVE damage and failure [17]. In the offline stage, a three-step approach is introduced: (1) data collection, such as collecting strain concentration tensor for each voxel in the RVE; (2) Unsupervised learning, which classifies all voxel elements into different clusters; (3) Generating cluster-wise interaction tensors. In the online prediction stage, cluster-wise strain responses are identified by solving a discretized Lippmann–Schwinger equation. A previous publication [16] shows that the SCA drastically reduces computational expenses, and the accuracy is verified against a high fidelity Direct Numerical Simulation (DNS). Therefore, the three-step two-stage data-driven SCA method is a valuable tool in the ICME process for modeling UD CFRP composites.

In this paper, the ICME modeling framework for UD CFRP structure performance prediction is presented. Under the framework, the macroscale UD model is discretized with an FE mesh. The UD microstructures are characterized by RVEs. RVEs are compressed into UD Reduced Order Models (ROMs) and provide mechanical responses for all integration points on-the-fly. The constitutive response of each constituent, e.g., fiber and matrix, is obtained from physical tests. The UD ROMs capture elastic and elasto-plastic responses of the UD CFRP through computing the RVE responses [18–20]. Moreover, the UD non-linearity due to matrix plasticity differentiates this work from previous efforts in CFRP ICME modeling, such as [21–23] and [24,25]. In those previous works, structural analysis is made by assuming linear elastic material responses. The UD ROMs compute RVE responses efficiently enough to replace the phenomenological anisotropic material model [26] and minimized material constants calibration effort.

In this manuscript, a predictive ICME framework, enabled by the data-driven ROM approach, is introduced for modeling UD CFRP laminate structure performance. Experimental validations are provided for all test cases. The methodology developed can be popularized for predicting performance of fiber reinforced polymer in general. The rest of the paper is organized as: Section 2 provides basic materials information. Section 3 discusses the experimental procedures of the UD CFRP coupon off-axial tensile test and the UD CFRP 3-pt bending test. Section 4 presents ICME modeling process for the UD CFRP in details. Section 5 will present results and experimental validation. Section 6 concludes the paper with several future directions.

Table 1
Carbon fiber elastic material constants.

E_{11}	$E_{22} = E_{33}$	$G_{12} = G_{13}$
245 GPa	19.8 GPa	29.2 GPa
G_{23}	$\nu_{12} = \nu_{13}$	ν_{23}
7.5 GPa	0.28	0.32

2. Materials information

In this section, the material properties obtained for A42 carbon fiber from DowAksa and thermoset epoxy resin from Dow chemical are provided. Material properties provided in this section are used through out the modeling work in this manuscript.

The fibers elastic constants are given in Table 1. Fibers are assumed to behave elastically. The fiber direction compressive strength is assumed to be one-fourth of the tensile strength, where the tensile strength (TS), according to the DowAksa official website, and compressive strength (CS) are assumed to be 4200 MPa and 1050 MPa, respectively. The choice of compressive strength is based on [27,28], which suggest the fiber compressive strength should be 10–60% of the fiber tensile strength. Ductile damage model for carbon fibers is assumed, as shown in Eq. (1), where $d_{fiber} = 0$ means no damage and $d_{fiber} = 1$ means fiber is damaged.

$$d_{fiber} = \begin{cases} 0, |\sigma_{11}| \le TS/CS \\ 1, |\sigma_{11}| > TS/CS \end{cases} \tag{1}$$

The epoxy resin elastic constants and tensile and compressive strengths are given in Table 2. The tensile and compressive yielding

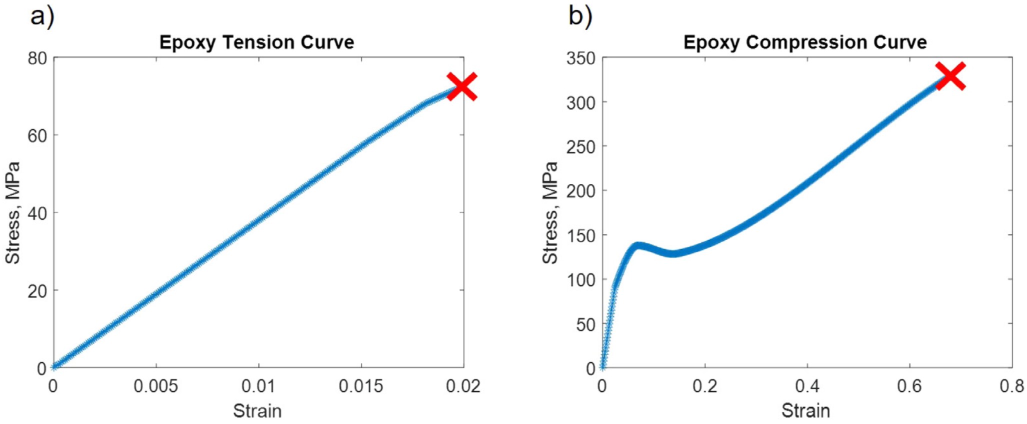

Fig. 2. Epoxy matrix (a) Tension stress versus strain curve and (b) Compression stress versus strain curve.

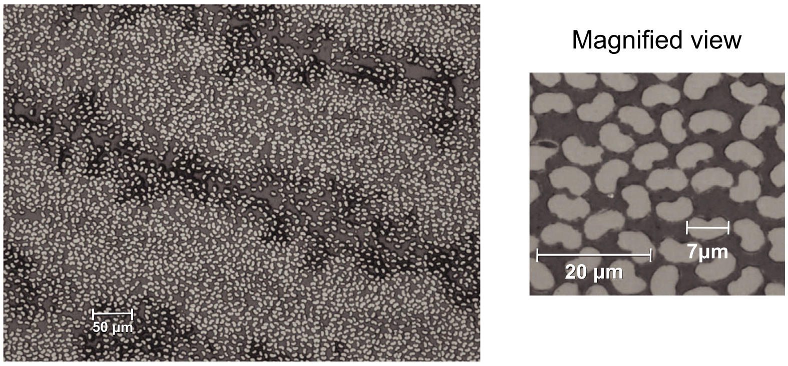

Fig. 3. Cross-section of UD CFRP under microscope, with magnified view shown on the right.

Table 2
Material constants of epoxy matrix.

E	ν	σ_T	σ_C
3803 MPa	0.39	68 MPa	330 MPa

curves are given in Fig. 2(a) and Fig. 2(b), respectively. The matrix compression test is performed according to the ASTM D695 standard. The compression test specimen exhibits a barreling effect during the test, causing excessive shear in the matrix, leading to final failure. Different tensile and compressive behavior suggest that a paraboloid yielding criterion can be implemented to capture such behavior. Readers are referred to [20] for details of the plasticity return mapping and epoxy damage algorithm.

3. Experiments for the UD CFRP

Material characterizations provide a good understanding of the material of interest. Various testing methods deliver the CFRP properties [29,30] and provide validation data for the prediction made by the ICME framework. In this work, two types of experiments are identified for examining the predictivity of the proposed UD CFRP ICME framework: (1) UD coupon 10° off-axial tensile test and (2) UD 3-pt bending test. This section gives experimental procedures for both tests listed above.

The cured UD CFRP lamina plaque is manufactured by Dow Chemical and the cross-section of the UD CFRP under microscope is shown in Fig. 3. Fibers are shown in lighter color and epoxy is shown in dark color. The fibers are randomly dispersed in the epoxy resin matrix, with overall volume fraction of 50%.

3.1. UD CFRP coupon 10° *off-axial tensile test*

The UD CFRP coupon specimen is prepared through the following steps. The edge of the UD plaque (with nominal fiber volume fraction of 50%) served as reference for the determination of the angle for cutting the 10° off-axis orientation. The specimen head areas and the tab (woven fiberglass in an epoxy resin) surfaces (with a length of 50 mm) were prepared with grinding paper before applying a commercially available acrylic adhesive. Metallic wires with a diameter of approximately 220 µm were used as spacers between specimen and the tab surfaces. The tabbing angle of about 16° was formed by grinding. The specimens were cut with a waterjet system to a nominal width (w) of 12.7 mm with a length of 210 mm for a resulting aspect ratio of 9 in the gauge section of length l = 120 mm, see Fig. 4 (specimens 001-005). An abrasive grit size of 220 µm and the lowest translation speed was chosen for minimal fabrication damage, based on preliminary studies for optimization of the waterjet cutting parameters (i.e., nozzle diameter, pressure, speed, abrasive grit size, etc.).

The displacement-controlled tensile tests have been conducted on a servo hydraulic testing machines at a quasi-static loading rate of 0.0167 mm/s (1 mm/min). The loading has been induced by the actuator located at the bottom of the test frames. Before each test, a precision steel block had been used for rotational alignment of the actuator to reduce out-of-plane misorientation. The specimens were rigidly hydraulically gripped with anti-rotation collars installed using diamond jaw surfaces and a pressure of 4 MPa. The gripping length on each side ranged between 30 mm to 40 mm. The specimens have been aligned with specimen stops in the grip.

All specimens were prepared for Digital Image Correlation (DIC) measurement with commercially available matte white spray paint, followed by applying matte black spray paint to create a random

Fig. 4. UD CFRP plaque (approximately 300 mm x 300 mm) with fibers oriented in the vertical direction, and the tabbed specimens after waterjet cutting.

pattern by the overspray method, see Fig. 5(a). The region of interest for strain measurement is shown in Fig. 5(b).

For stereo-DIC measurement, two 4.1 Mpx (2048 px x 2048 px) cameras and 35 mm fixed focal length lenses were used. The image acquisition rate was 2 Hertz. The resolution was 60 μm to 70 μm per pixel and the size of the dark speckles was about 232 μm ($\sim$3.4 px), measured via the line intersection method. The dark/bright ratio of the sample was nearly one (54:46). According to [31], the subset size should be at least three times the average speckle size. For data analysis, the chosen subset size was 15 px and the step size was 6 px. The reference image has been taken at a force $F = 0$ kN while the specimen has only been clamped by the top grip. For analysis, engineering strain has been calculated using a commercially available DIC software package. A more detailed investigation on 10° off-axis testing can be found in [32].

3.2. *UD CFRP hat-section dynamic 3-pt bending test*

The UD CFRP hat-section studied in the current work was molded with A42 fibers, provided by DowAksa, and thermoset epoxy resin with fiber volume fraction of 50%. The geometry of the dynamic 3 point bending test sample was shown in Fig. 6(a). The nominal thickness of the hatsection was 2.4 mm with about 0.2 mm thickness of each layer. The hatsection sample was deformed in a hot compress and held for about 5 min for curing. The hatsection was made with [0/60/−60/0/60/−60]s layup (noted as 0–60). In order to perform the test successfully, a back plate of the same layup and thickness was glued to the bottom of the hatsection sample with Betamate 4601 glue (Dow), as shown in Fig. 6(b).

The setup of the dynamic 3 point bending test was shown in Fig. 6(c). The sample was slightly fixed to the lower roller (diameter 25 mm) with tape in order to allow the rotation at the bottom. An impactor with 25 kg mass and 100 mm outer diameter impacted the hatsection with initial impact velocity of 4.66 m/s. The peak impactor acceleration and the impactor force were recorded for comparison to the numerical predictions.

4. UD CFRP ICME modeling process

In the ICME framework, the CFRP structure is modeled in a bottom-up fashion, as introduced in Fig. 1. At the microscale, UD CFRP microstructure is modeled as RVEs. RVEs are compressed into the microstructure database, which contains ROMs for all RVEs. ROMs can be fed into an arbitrary macroscale FE model composed of 3D stress state elements, such as the brick element or the thick-shell element. The ROMs interact with the macroscale model and enables a multiscale model with information exchange between the microscale and the macroscale. In this section, the multiscale modeling workflow for the ICME process is provided step by step.

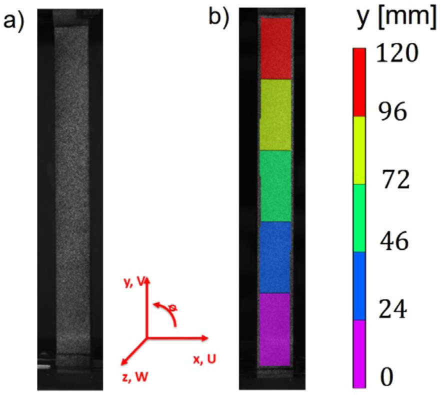

Fig. 5. (a) Field of view with speckle pattern on specimen with l = 120 mm, w = 12.7 mm; (b) Region of Interest (colored area) for data analysis. (For interpretation of the references to color in this figure legend, the reader is referred to the web version of this article.)

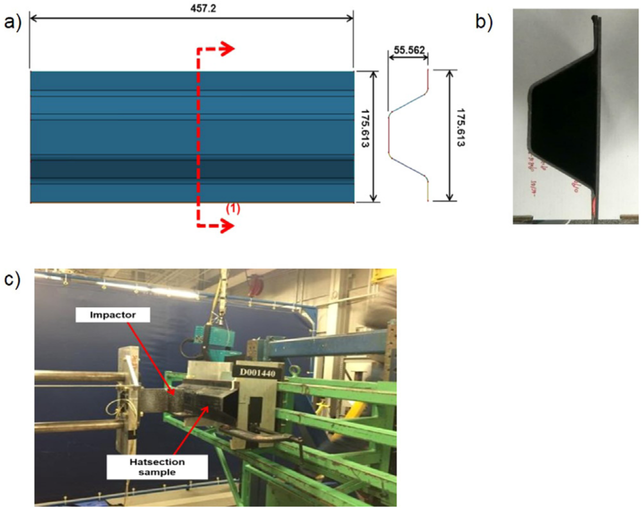

Fig. 6. UD CFRP hat-section sample: (a) geometry; (b) sample with back plate; (c) dynamic 3 point bending test setup. Experimental results are provided in Section 5.

4.1. *ICME multiscale modeling work flow*

For the illustration of ICME multiscale model setup, the UD CFRP coupon specimen geometry described in Section 2 is used. The UD CFRP coupon FE model mirrors the real UD CFRP coupon made in Section 2. It replicates the off-axial tensile experiment performed as a one-to-one replica. The FE model contains all 12 UD CFRP laminae. Each of these laminae is modeled as a singular layer of thick shell elements with 2 integration points in the thickness direction (Z direction), as shown in Fig. 7. For clarity, the FE model has been magnified by a factor of 2 in the thickness direction. The FE model contains 49,420 elements and 99,480 integration points. The magnified region in Fig. 7 shows four selected thickshell elements and integration points in each element. The UD CFRP microstructure, modeled by the UD CFRP RVE, is assigned to each integration point in order to compute material responses under external loadings.

To illustrate the diversity of the microstructure database, two selected integration points, marked by the red box in Fig. 7, are further magnified for the underneath microstructure. Fig. 8 depicts how two UD RVEs from two neighboring integration points (as indicated by the solid red box) are modeled using the microstructure database. The database contains four different RVE setups that could potentially be used for the multiscale modeling process. On the right side of Fig. 8,

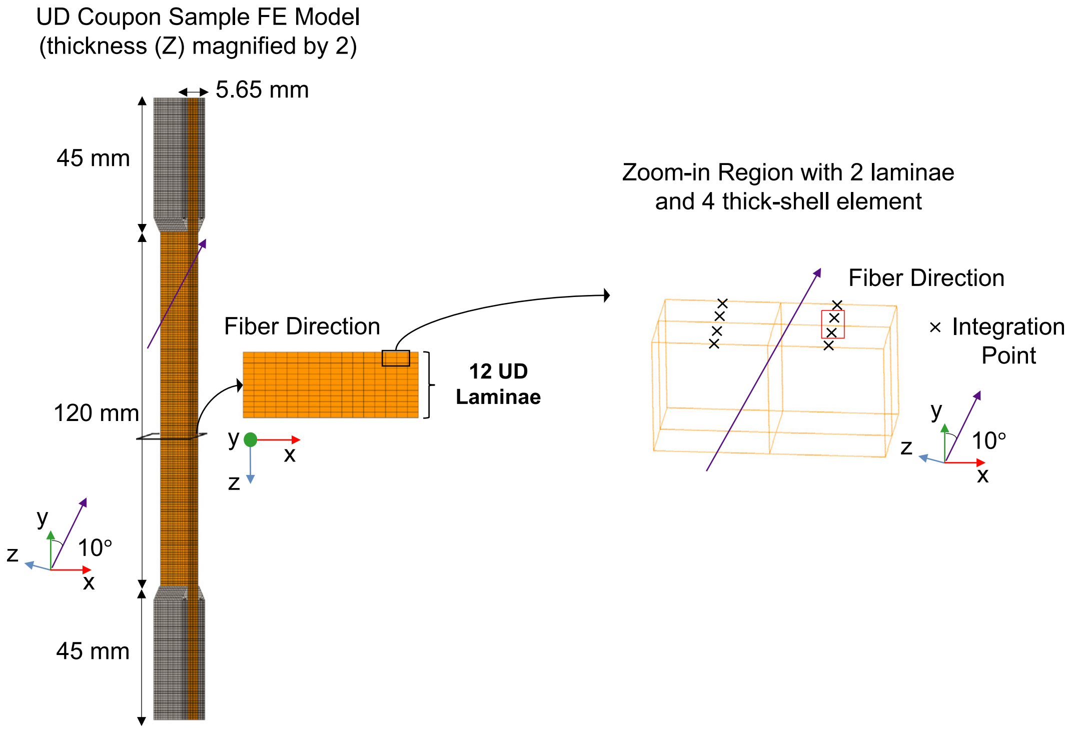

Fig. 7. UD CFRP coupon FE model setup. In this setup, the material responses at each integration point (marked as black cross) is computed using a UD RVE.

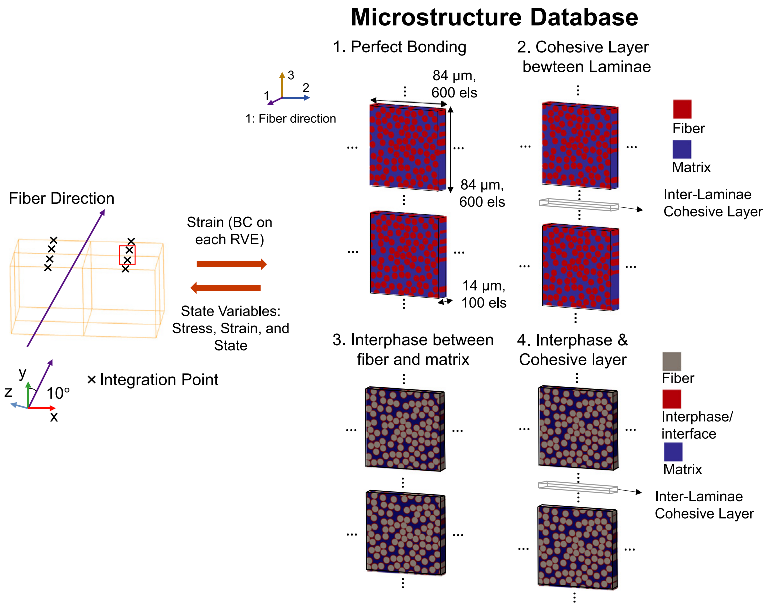

Fig. 8. Four candidate microstructure setups in the database for the UD coupon specimen: (1) UD with perfectly bounded fiber and matrix (2) Assuming a cohesive layer between UD laminae (3) UD with interphase between fiber and matrix (4) UD with interphase between fiber and matrix, as well as a cohesive layer between UD laminae. The database is designed so that users can assign various microstructures to the macroscale model based on their needs. 'els' in this figure stands for voxel elements in the RVE. The UD microstructure Setup (1) is used in the present work.

the ellipses around each RVE are used to indicate that there are hidden neighboring RVEs on each side of the RVE due to the assumption of periodic boundary condition (PBC). The first setup assumes perfect bonding between the fiber and matrix, as well as for all laminae. The second setup assumes a weak bond between laminae that can be modeled as a cohesive layer. The third setup assumes an interface region between fiber and matrix, which is modeled as non-zero thickness interphase. The fourth setup assumes there is an interface region between fiber and matrix and that there is weak bond between the laminae. In this work, only the first setup is incorporated due to the assumption of perfect bonding.

The RVEs illustrated in Fig. 8 are compressed into UD CFRP ROMs through the three-step offline data compression stage. Details on the offline stage will be provided in later subsections.

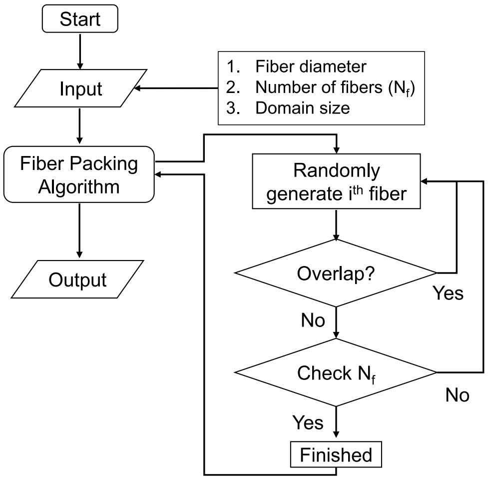

Fig. 9. Algorithm flow chart for generating UD RVE using Monte Carlo method.

4.2. UD RVE modeling

The UD RVE used to characterize the UD CFRP microstructure is simplified compared to the real material, which is shown in Fig. 3. First, as shown in Fig. 3, the fibers do not have a perfect circular cross-section, but rather a bean-shaped cross-section. As shown in the right side of the same figure, this bean shape can fit in an ellipse of major axis of 7 μm. To generate the UD RVE, the fiber cross-section is simplified as a circular shape with a diameter of 7 μm, and the fiber is assumed to be perfectly straight. The fiber geometry does not affect the predicted properties when comparison with test data is made, as can seen in [22]. Second, when the RVE is large enough, typically ten times the fiber diameter, the random distribution of fiber does not affect the RVE responses significantly [33]. Therefore, an RVE size of 84 μm is chosen.

The cross-section of the UD RVE can be modeled in a 2D fashion, where the Monte Carlo method is used to pack circles randomly in a 2D domain until the target fiber fraction is met. If part of any fiber lies outside four edges of the RVE, that part will reappear in the opposite directions to ensure periodic distribution of all fibers so the RVE complies with the PBC assumption. The generated 2D mesh is then discretized by square pixels. The algorithm flow chart for generating a 2D mesh of the UD RVE is given in Fig. 9. The RVE algorithm discussed above is suitable for UD RVEs with fiber volume fraction around 50%. For higher volume fractions, specialized algorithms are needed. This is beyond the scope of current work and is not discussed in detail. Finally, the 2D mesh is extruded by assigning thickness to all pixels to generate a 3D voxel mesh.

The generated UD RVE is given in Fig. 10. The RVE has a resolution of 600 by 100 cubic voxels with voxel edge length of 0.14 μm. 93 fibers are generated in the RVE.

To utilize UD RVE for compute stress responses on-the-fly in a macroscale FE model, the ROM technique is used to compress RVEs into a microstructure database. The ROM process is given in following sections.

A DNS of RVE transverse tensile loading is also performed. The DNS is used to verify the efficacy of the ROM, which is supposed to produce accurate results compared with DNS solution. Fiber and matrix properties are following data given in Section 2

4.3. Reduced order modeling of UD RVE

The aforementioned UD RVE contains significant DOFs for a single RVE run due to the fine mesh resolution. To model the UD CFRP structure with UD RVEs, the computational cost is not affordable due to the costly RVE computation. Instead, the ROM technique is applied to the UD RVEs to generate their ROMs. The ROM, in theory, will reduce the computational cost significantly compared to RVE computation. The SCA approach is used to generate the ROMs for the UD RVEs. All necessary derivations for SCA are provided in Appendix A. In this subsection, we will focus on illustrating the 3-step offline stage computation and the online prediction stage.

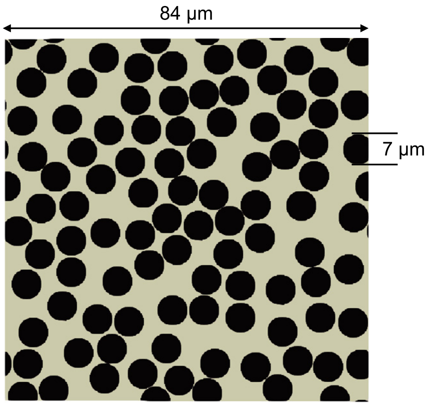

Fig. 10. The UD RVE Generated by Monte Carlo method.

4.3.1. Offline

The offline stage starts with a high fidelity RVE discretized by a voxel mesh. The strain concentration tensor $\boldsymbol{A}(\boldsymbol{x})$ links macroscopic strain applied on the RVE to each voxel through the following relationship:

$$\boldsymbol{\varepsilon}^{\boldsymbol{m}}(\boldsymbol{x}) = \boldsymbol{A}(\boldsymbol{x}) : \boldsymbol{\varepsilon}^{\boldsymbol{M}} \tag{2}$$

where $\boldsymbol{\varepsilon}^{\boldsymbol{m}}$ is the microscopic strain at any voxel in the RVE and $\boldsymbol{\varepsilon}^{\boldsymbol{M}}$ is the applied macroscopic strain of the RVE. $\boldsymbol{A}(\boldsymbol{x})$ is the well-known strain concentration tensor. Under the Voigt notation, $\boldsymbol{\varepsilon}^{\boldsymbol{m}}$ and $\boldsymbol{\varepsilon}^{\boldsymbol{M}}$ are both 1 by 6 vectors. This means $\boldsymbol{A}(\boldsymbol{x})$ is a 6 by 6 matrix. $\boldsymbol{A}(\boldsymbol{x})$ can be computed by applying six orthogonal loading conditions where $\boldsymbol{\varepsilon}^{\boldsymbol{M}}$ has only one non-zero component at a time. This would allow $\boldsymbol{A}(\boldsymbol{x})$ to be computed one column at a time, and six loading conditions can provide all 36 components of $\boldsymbol{A}(\boldsymbol{x})$.

Once $\boldsymbol{A}(\boldsymbol{x})$s for each voxel are computed, unsupervised learning can be applied to all $\boldsymbol{A}(\boldsymbol{x})$s within the RVE to perform clustering. This process will compress the original RVE made of many voxel elements into several clusters. For UD RVE with fiber and matrix phases, fiber and matrix phases are decomposed separately. Number of clusters in fiber and matrix phases are denoted as K_f and K_m, respectively. It is convenient to define $K_f + K_m = K$. The clustering process for UD RVE setup one and two, as depicted in Fig. 8, is given in Fig. 11. The data compression process is performed using an unsupervised learning method, such as K-means clustering.

Interaction tensors $\boldsymbol{D}_{IJ}$ must be computed between all cluster pairs. For the sake of simplicity, readers are referred to previous publications: [5,16]. Once interaction tensors are computed, it is possible to solve for cluster-wise strain increments by solving the discretized Lippmann–Schwinger equation.

4.3.2. Online

The online stage involves solving the following residual form in Eq. (3). Details of the SCA online stage is given in Appendix A.

$$r^I = -\Delta\varepsilon^M + \Delta\varepsilon^I + \sum_{J=1}^{K} \left[\boldsymbol{D}^{IJ} : (\Delta\sigma^J - \boldsymbol{C}^0 : \Delta\varepsilon^J) \right], \quad I = 1, 2, 3, \dots, K \tag{3}$$

where r^I is the residual of strain increment on each cluster. The residual can be minimized by first linearizing the Eq. (3) with respect to $\Delta\varepsilon^I$

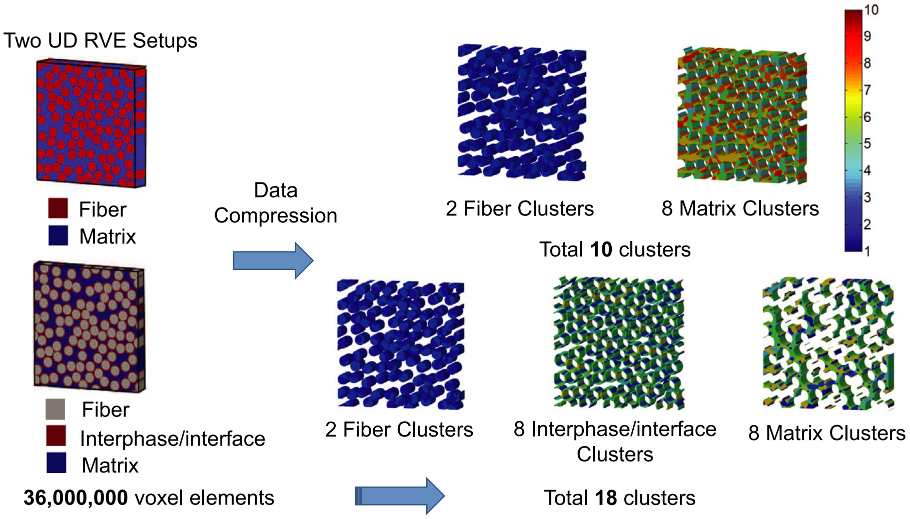

Fig. 11. UD RVE clustering process for setup 1 and 2 from Fig. 8.

and solve for $\Delta\varepsilon^I$ that minimizes r^I. Details of the derivation process of Eq. (3) and linearization are given in Appendix A.

Note that in the present multiscale modeling scheme, ROMs are deployed on all integration points in the FE mesh of the composite laminate structure. At each integration point, the macroscopic strain increment $\Delta\varepsilon^M$ is provided by the FE solver and the cluster-wise stress and strain responses are solved with Eq. (3). The homogenized RVE stress increment, denoted as $\Delta\sigma^M$, is returned back to the FE solver.

4.3.3. DNS vs. reduced order model

Three sets of ROMs of the UD RVE are generated with a different number of clusters: (1) 1 clusters in the fiber phase (K_f =1) and 4 clusters in the matrix phase (K_m = 4) (2) 2 clusters in the fiber phase (K_f = 2) and 8 clusters in the matrix phase (K_m = 8); (3) 16 clusters in the fiber phase (K_f = 16) and 16 clusters in the matrix phase (K_m = 16).

To verify that the ROM will produce satisfactory results, a transverse tensile test with maximum 0.02 strain magnitude is performed. The same loading is applied to three ROMs as well. Stress and strain curves for all three cases are plotted in Fig. 12. The DNS result is plotted with a 95% confidence interval. The results of three ROMs mentioned earlier are denoted as, "SCA, 4 clusters", "SCA, 8 clusters" and "SCA, 16 clusters" respectively. From the results shown in Fig. 12, it is clear that ROMs with 8 and 16 clusters converge to the DNS solution, but the ROM with 4 clusters deviates from the DNS solution when the strain is larger then 0.015. To save computational cost in the concurrent multiscale modeling of the UD CFRP and preserve adequately the RVE local evolution, the ROM with 8 clusters is used in the following structural level models.

As mentioned in Section 2, a paraboloid yielding function is implemented to consider different tensile and compressive behavior of the epoxy matrix. The matrix damage is modeled using a paraboloid epoxy damage model.

The UD ROM utilizes fiber and matrix to compute UD CFRP's material responses efficiently. In the UD structure modeling, an equivalent damage model is applied to all ROMs to simulate the damage of RVEs. The damage of the RVE at each integration point will reduce load carrying capacity of each element in the macroscale model. When the damage exceeds 0.5, the integration point will lose load carrying capacity. The macroscale element will fail when all integration points in the element have lost load carrying capacity.

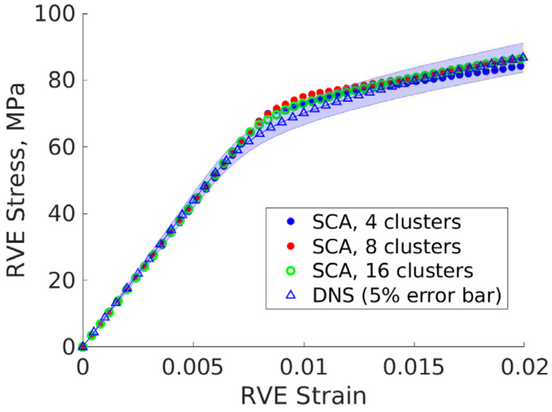

Fig. 12. Transverse tension results of DNS and ROMs. The DNS result (computed from FEM) has an error bar representing a $+/-5\%$ interval from the DNS result. The results of ROMs computed from SCA are close the interval, suggesting good accuracy demonstrated by the ROMs..

4.4. UD CFRP coupon off-axial tensile simulation model setup

With all aforementioned information available, the UD CFRP Coupon specimen multiscale model is illustrated in Fig. 13. The applied boundary condition is shown in Fig. 13. In the experiments, both tab sections are tightly clamped with a pressure of 4 MPa. The same clamping pressure is applied to both tab sections of the FE model. Moreover, the two surfaces of the upper tab section are fixed in the y direction, but the two surfaces of the bottom tab section are allowed to move in the y direction. A displacement towards the negative y direction is applied to the bottom tab section so the coupon is extended, allowing the tensile test to be repeated. One can see the FE coupon specimen model preserves most of the experimental conditions. This aligns with the purpose of ICME modeling, where a real-world part is modeled a nd analyzed with as many details as possible.

4.5. UD CFRP dynamic 3-point bending model setup

The 3-point bending model [34] is the second test case for validating the efficacy of the proposed framework of UD CFRP. A similar approach to the UD CFRP coupon model is adopted. The model of the UD CFRP hat-section is shown in Fig. 14, where a $[0/60/-60/0/60/-60]_s$ layup is used. As shown in the Figure, the 12 layers of the UD laminate structure

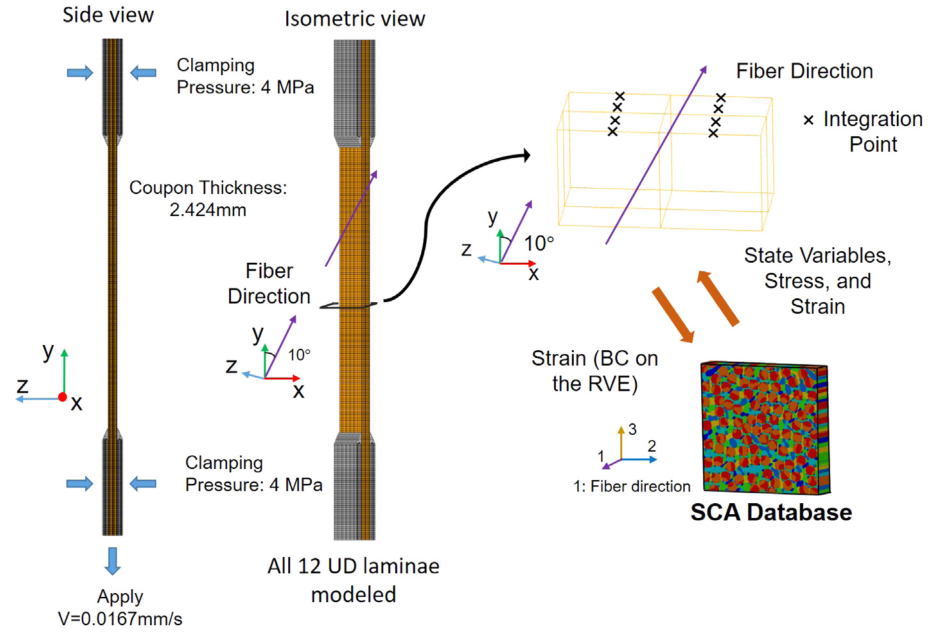

Fig. 13. UD CFRP coupon off-axial tensile simulation setup.

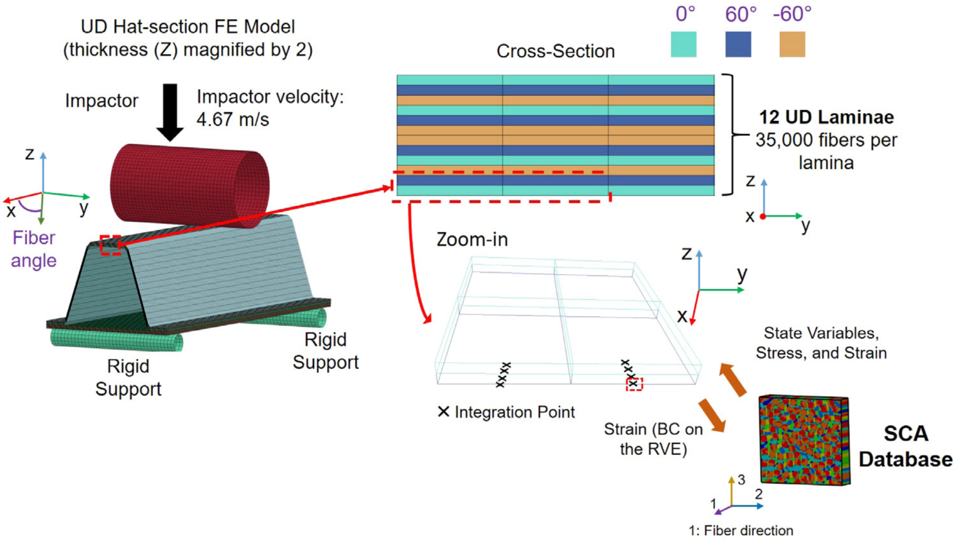

Fig. 14. UD CFRP dynamic 3-point bending model setup.

are modeled explicitly with thick shell elements. Such a setup allows for the capturing failure of individual lamina under the effect of the impactor.

Up to this point, all necessary modeling steps of the UD CFRP structure are finished. The concurrent multiscale modeling framework is applied to test problems mentioned in Section 3. All test problems are modeled with realistic geometries, hence the FE model utilizes the same boundary conditions given in both tests. The experimental test data is used for validating the proposed UD CFRP concurrent multiscale modeling framework. The prediction capability of the framework is examined against experiments conducted delicately. The results of both test problems and associated discussion are given in the next section.

5. Results and discussion

Concurrent simulation results of the off-axial coupon tensile test and the 3-point bending test are discussed in this section. The same UD RVE shown in Section 3 is used in both cases due to same fiber volume fraction.

5.1. *UD CFRP coupon off-axial tensile simulation*

In this section, the concurrent multiscale 10° UD off-axial coupon specimen tensile simulation results are presented and compared against experimental results. The coupon model geometry is given in Section 3 Figure. A loading rate of 0.0167 mm/s gradually extends the coupon sample in the downwards direction. During the deformation process, a 10° stress band is formed as one can see in Fig. 15. The UD CFRP

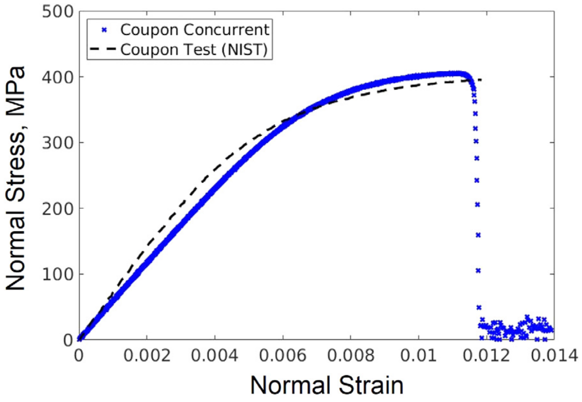

Fig. 15. UD coupon normal stress vs. normal strain. The comparison shows the prediction is in a good match with the test data. The difference between prediction and experimental result is potentially caused by the microstructure variation in the real UD material.

Table 3
Predicted maximum normal stress and strain of the off-axial UD coupon sample.

	Maximum normal stress (MPa)	Maximum normal strain
Experiment	395.64	0.012
Prediction	404.81	0.011
Difference	**2.32%**	**8.33%**

coupon off-axial tensile simulation is used to validate that the proposed multiscale modeling framework for UD CFRP material predicts the system behavior with good accuracy.

The comparisons between multiscale coupon simulation and the test data are made for: (1) normal stress vs. normal strain; (2) y direction displacement; (3) y direction strain. Based on the comparisons, two purposes are addressed: (1) To validate the multiscale modeling framework for the UD CFRP material; (2) To demonstrate that the present UD CFRP multiscale model has considerable prediction capability.

For the FE model, the normal stress is computed using the reaction force computed at the gauge cross-section area divided by the area of the original coupon cross-section. The reaction force of the cross-section near the top tab region of the coupon was recorded during the simulation. The reaction force is then used to compute the normal stress of the multiscale model. The change of the gauge length was used to compute normal strain. Normal stress versus strain of the multiscale model is plotted as blue dots in Fig. 15.

Comparing the stress and strain curves from the multiscale model and the experimental data, a good match is observed. The prediction has same trend as the experimental data, as shown in Table 3. The predicted maximum stress is 404.81 MPa, which is close to 395.64 MPa reported from the experimental data. In addition, the maximum strain predicted by model is 0.011, which again is in a good match with experimental measured value of 0.012. Both predicted quantities of interest are within 10% deviation from experimental measurements, meaning the UD CFRP concurrent multiscale model is validated against the experimental data.

The y direction displacement and strain fields are validated with experimental results, as shown in Fig. 16(a) and (b), respectively. The black arrows in Fig. 16(a) represent the vertical distance between fringes from −0.250mm and −0.700 mm. The prediction made by the multiscale model is 80.26 mm, with a 3.95% difference to the DIC measurement of 83.57 mm. As shown in Fig. 16(b), the y direction strain yield contour predicted is quite similar with the DIC measurement. Both strain field contours show a clear band across the middle of the coupon. The DIC strain field is highly non-uniform due to unavoidable microstructure variation during manufacturing process. Still, the results are encouraging since the predicted displacement and strain fields agree with experimental results. Due to the coupon has all fiber align in the 10° orientation, the coupon is primarily under shear deformation as a result of the given fiber orientation. A good match of the UD coupon stress and strain curve suggests that the UD RVEs embedded at the lower scale capture the combined tension and compression responses of the UD material. Therefore, the 10° coupon simulation serves as a proper test-bed for validation purpose as it creates complicated loading conditions upon UD materials, whose responses are accurate predicted using the present method.

Moreover, the predicted crack formation and the actual coupon crack formation are depicted in Fig. 17(a) and (b), respectively. In both Fig. 17(a) and (b), the crack propagates all the way across the coupon gauge section. The pattern of predicted crack is not an exact replica of the experimental results because the numerical model has yet to take local microstructure variation into account, as depicted in Fig. 3. In the future work, the local microstructure variation will be considered in the modeling process to address the uncertainty effect on the macroscopic performance. Nonetheless, the ICME model is able to provide an accurate prediction of the maximum stress and strain of the coupon sample, as reported in Table 3, as well as a prediction of the failure pattern. The prediction made by the ICME model is consistent with the experimental observation, which provides confidence for the predictivity of the proposed multiscale modeling scheme for the ICME process.

The ICME multiscale modeling scheme has been validated by the experimental data discuss above. However, the capability of the proposed multiscale modeling scheme is beyond providing accurate prediction of the macroscale quantities. It also provides detailed microstructure evolution of UD CFRP structure for studying the root cause of the failure in the UD coupon.

Fig. 18 is used to illustrate the local UD CFRP damage process using three snapshots. The magnified views of the region marked in red are shown in Fig. 18(a), (b), and (c) at y displacement of 1.40 mm, 1.41 mm, and 1.42 mm. The UD RVEs representing elements marked in black are shown in Fig. 18 (d), (e), and (f). In Fig. 18 (e), all three RVEs are experiencing matrix damage, suggesting the potential cause of coupon failure. In Fig. 18 (b), the bottom element has a stress contour turning to blue–green from green, suggesting reduced load carrying capacity. This is due to aggravated matrix failure of the middle and bottom RVEs as shown in Fig. 18(e). In Fig. 18(c), the middle and bottom elements have been marked as failed due to the loss of load carrying capacity, whereas the top one is still capable of carrying load. However, as shown in Fig. 18(f), the top RVE is also experiencing severe matrix damage, which means this RVE will fail shortly. The UD RVE microstructure evolution in Fig. 18 provides valuable information in the understanding of microscale damage process. Moreover, the UD RVE stress and damage evolution are captured simultaneously as the macroscopic UD coupon simulation. In the future, in-situ monitoring techniques can be combined with the existing modeling capability to further validate microstructure failure process of the UD.

The computational efficiency of the present ICME scheme compared with traditional multiscale modeling method, FE^2, is given in Table 4. The simulation time of FE^2 is estimated based on DNS calculation time of the UD RVE. It can be seen that a 5272 speed-up is achieved using the present scheme. Note that FE^2 would necessarily require storage of lower scale UD RVE DNS mesh, resulting in extra storage/RAM cost. Under the ICME scheme, the UD RVE evolution is reconstructed from the reduced order model, which drastically eliminates such need.

Using detailed microstructure evolution information illustrated in Fig. 18, a path towards UD CFRP design is discovered. For example, one can design matrix strength to avoid matrix damage at small loading magnitude. Or, one can design interphase properties and incorporate the interphase region into the model to examine the interphase effect and the delamination behavior of the UD CFRP.

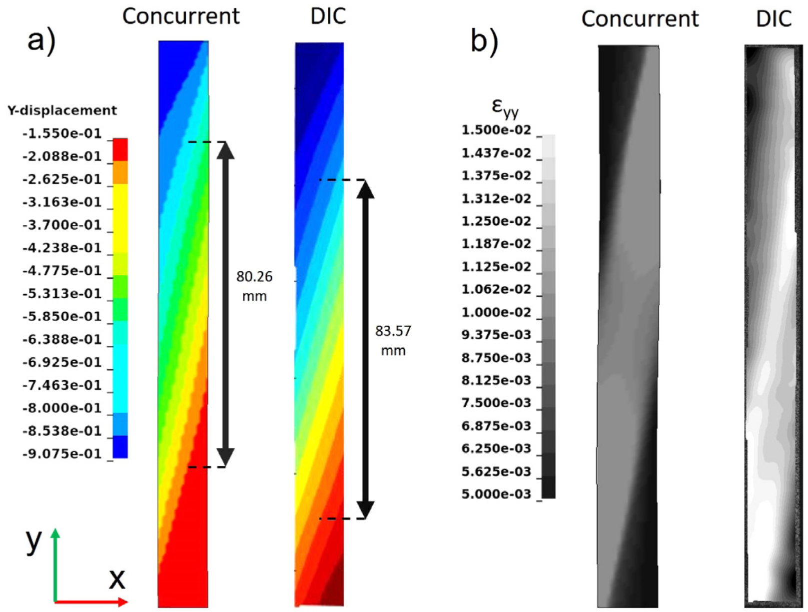

Fig. 16. Contour of (a) Y displacement and (b) Y strain field. The applied displacement on prediction and DIC is 0.9031 mm. In the displacement plots (a), two black arrows measure the vertical distance between fringes from −0.250 mm and −0.700 mm and the difference is 3.95%. In the gray scale strain contour (b), the predicted strain field is comparable to the DIC one. The difference the predictions and the DIC images is caused by microstructure variations in the real UD CFRP material, which can cause strain concentration in the real sample.

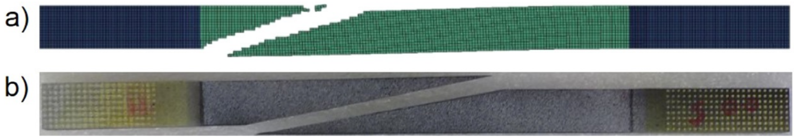

Fig. 17. The coupon crack formation of (a) numerical prediction and (b) experimental result. Since the numerical model assumes perfect materials without microstructure variations, the predicted pattern deviates from the test result.

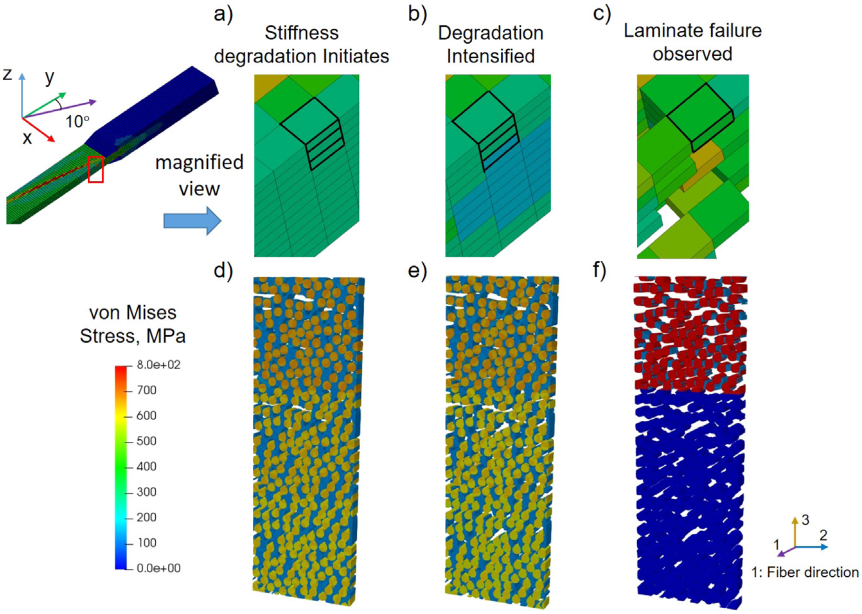

Fig. 18. Magnified view of coupon local microstructure for marked macroscale elements at (a) d_y=1.40 mm; (b) d_y=1.41 mm; (c) d_y=1.42 mm and local UD RVEs at (d) d_y=1.40 mm; (e) d_y=1.41 mm; (f) d_y=1.42 mm. All RVEs are shown in undeformed configuration.

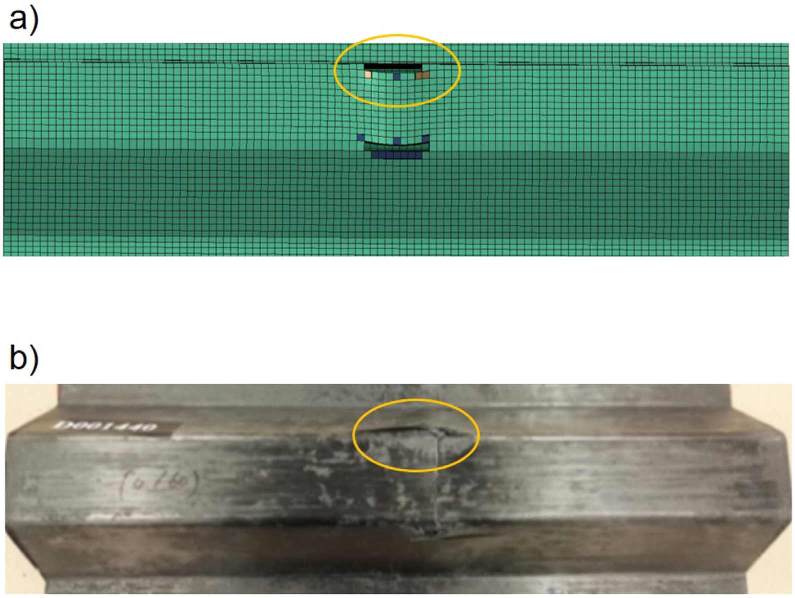

Fig. 19. UD hat-section after the impact from (a) Prediction (b) Experiment. The damaged zones on the sidewalls are marked by yellow ellipses. It can be observed that the hat-section is being pushed inwards upon the impact, and the impactor will cause a dent on the hat-section.

Table 4
Comparison of total simulation time in CPU hr. for the concurrent simulation.

	FE^2 (estimated)	ICME approach
Simulation time (hr.)	3,093,055	540
Speed-up	–	5527

Table 5
Impactor peak load and acceleration.

	Peak load (N)	Peak impactor acceleration (m/s^2)
Experiment	10,328	0.39
Prediction	9480	0.379
Difference	**8.21%**	**2.82%**

5.2. UD 3-point bending model

To further illustrate the efficacy of the concurrent scheme, the UD 3-point bending model concurrent simulation is also performed. The fractured hat-section of the simulation and experiment is shown in Fig. 22. The UD 3-point bending simulation is used to examine the applicability of the proposed scheme to an arbitrary UD CFRP structure. Two quantities are chosen to make the comparison: peak load on the impactor and the peak impactor acceleration. Due to severe vibration of the hat-section in the 3-point bending simulation, the matrix has been simplified as an elastic material with brittle failure, where the failure strength is set to compression strength as defined in Table 2.

After the impact, the hat-section from the numerical prediction and experimental result are plotted in Fig. 19(a) and (b), respectively. The yellow ellipse marked damaged zones on the hat-section. It can be observed that the impact push material inwards, cause delamination of the hat-section on both side-walls. The similar trend observed in the numerical model and the experimental result further suggests the multiscale model can provide a good prediction of the failure pattern on the UD structure. The ICME process can be applied to predict the responses of a UD structure under complex loading conditions.

In addition to the good match of the UD structure deformation and failure, quantitative comparisons for peak load on the impactor and peak acceleration of the impactor are reported in Table 5 with comparison with the experimental data. A reasonable match between prediction and experimental data can be seen. Specifically, the relative differences of peak load and peak impactor acceleration are 8.21% and 2.82%, respectively. Both predictions are within 10% deviation from the experimental data, providing confidence that the macroscopic performance indices can be predicted with the ICME framework.

In Fig. 20, the impactor force evolution vs. loading time is presented. The prediction is consistent with the experimental data provided by the Ford Motor company. This suggests that the current ICME framework is suitable for predicting UD CFRP structure performance.

In Fig. 19(a), the failure of the hat-section is depicted at the macroscale. Underneath the complex macroscopic structure evolution, local RVE responses are captured in a concurrent fashion and provide extra information for the microscale evolution in the hat-section. To illustrate the von Mises stress evolution in the UD microstructure, RVEs representing three columns of elements shown in Fig. 21 are visualized. The three columns of elements are shown in the magnified view on the right of Fig. 21. Each column contains 12 layers of UD laminae, where each lamina is visualized with 1 UD RVE. The fiber orientation on each UD laminate is color coded as shown in Fig. 21. All UD RVEs are aligned with the fiber orientation as suggested by the color code, following the lamina orientation explained in Section 3.6. All UD layers are counting from layer 1 to layer 12 in the top-down fashion.

The hat-section deformation and von Mises stress contour under the impactor are shown in the upper half of Fig. 22. Three different snapshots were taken with the impactor and supports hidden at: upon impact; Impactor displacement of 4.85 mm; Impactor displacement of 6.85 mm. In the upper half of Fig. 22(a), the impactor contacts the hat-section and caused immediate stress concentration at the contact region. In Fig. 22(b) and (c), it can be observed that the top and two sidewalls of the hat-section bend inwards after the hat-section contacts the impactor. The impactor pushes the middle of the UD CFRP hat-section inwards, simulating the scenario where the composite structure is under the external loading condition.

Corresponding RVE von Mises stress contours are shown in the lower half of Fig. 22(a), (b), and (c). It can be seen that UD RVEs can be used to investigate the inter-laminate stress distribution of the UD microstructure. Due to different fiber orientations in the hat-section laminate structure, the von Mises stress magnitude varies from layer to layer across the thickness direction, which might lead to earlier failure for those layers with larger stress magnitude. The RVE plots shown in Fig. 22(b) suggested that the second and third in location

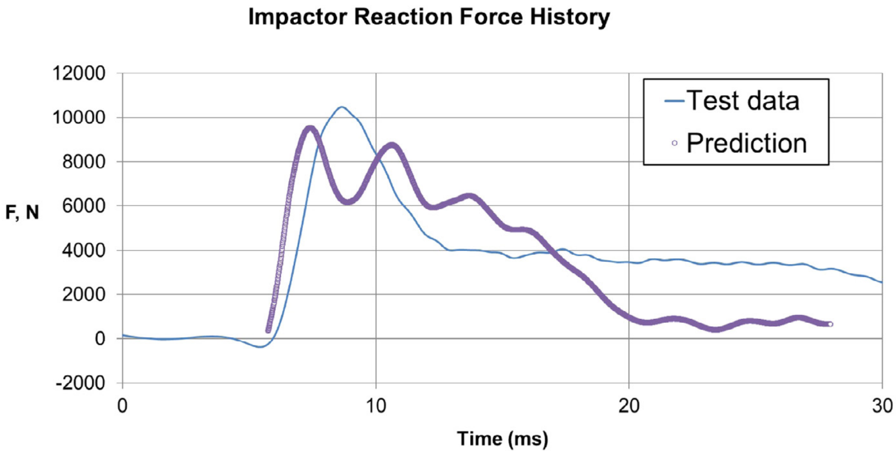

Fig. 20. UD hat-section impactor reaction force evolution vs. loading time. The simulation results shows good consistency compared to the experimental data. High-frequency data in the test data is filtered using the SAE filter with a sampling frequency of 180 Hz for the test data. A Similar procedure is applied to the prediction data. The oscillation observed is due to the high loading rate of the three-point bending problem. Note that during the experiment, the impactor is not in contact with the hat-section until 5.6 s later after release. This results in zero reaction force in the blue curve as shown in the figure.

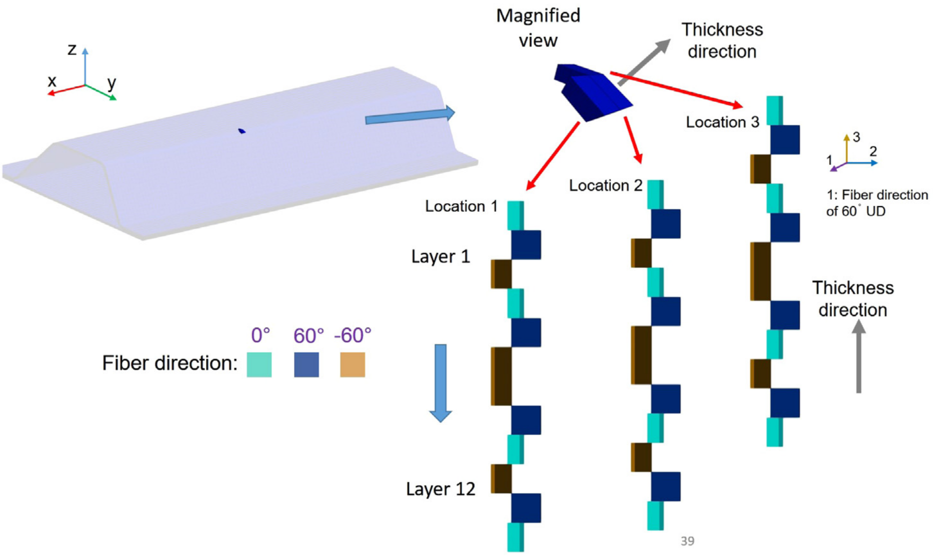

Fig. 21. UD hat-section mesh with magnified view of three columns of elements in the through-thickness direction. The impactor is hidden for clarity. This setup shows the location of three columns of elements (12 elements per column, representing all 12 layers of UD laminae) across the thickness direction in the UD hat-section mesh. Each element is represented by one UD RVE, whose fiber orientation matches with the UD layup given. All UD RVEs are color-coded according to the fiber orientation.

1 has much higher stress magnitude comparing with those in other layers. In Fig. 22(c), those two layers have reached failure as the stress magnitude are zero. This suggested that the multiscale modeling has great potential in predicting microstructural evolution in a complex UD CFRP laminate structure. Such information can be used to examine various UD CFRP laminate designs using the virtual verification capability to examine macro and micro material performance. This can assist the CFRP design process by eliminating designs that under-perform certain performance indices, or designs with undesired microstructural evolution pattern.

For UD CFRP materials, understanding the microstructure failure mechanism provides valuable information in improving CFRP design. Similar to the UD CFRP coupon model, the microstructure evolution of the hat-section is captured and illustrated in the three-snapshot view in Fig. 23 with different impactor displacement. In Fig. 23, two UD CFRP RVEs representing two marked regions are visualized. It can be seen that the RVE in the upper layer begins to damage while the RVE in the lower layer stays intact when d_y=5.91 mm, as shown in Fig. 23(a). When the upper layer fails, the neighboring region will collapse towards the newly formed empty region and the neighbor elements will compress the lower layer. Soon, the lower layer fails as well when d_y=6.13 mm, as shown in Fig. 23(b). Eventually, both layers fails as shown in Fig. 23(c). This three snapshots illustrate the ability of investing detailed microstructure evolution of UD CFRP for a structural level simulation. Such information can provide guidance for design of CFRP structure against local damage to improve the structural performance.

In this subsection, a one-to-one replica of the UD CFRP Coupon 10° off-axial tensile test multiscale simulation and the UD CFRP hat-section 3-pt bending test are resolved using the proposed multiscale modeling framework. Both models are validated against experimental data for validation of the framework. Predictions made by the numerical counterparts are all within 10% difference compared with experimental data. The agreement shows the current work can be used for prediction of other UD CFRP laminate structure. Moreover, the concurrent capture of microstructure evolution provides microstructure evolution history for any location in the FE model of the UD laminate. This allows researchers to look at the detailed microstructure evolution, which is

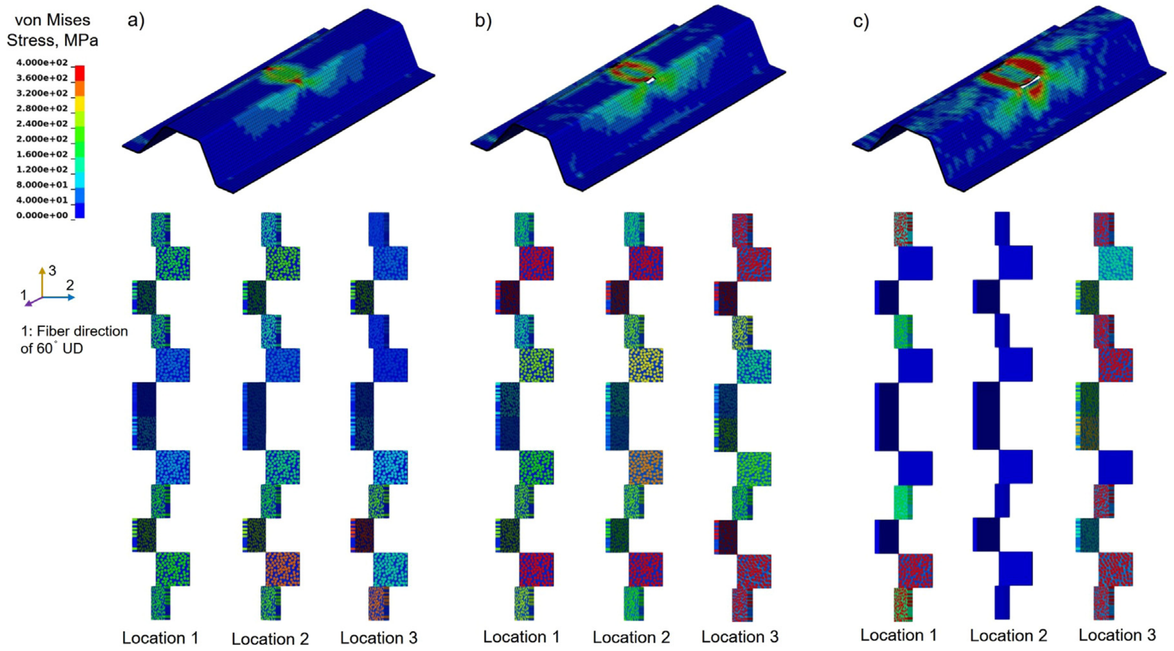

Fig. 22. Isometric view of the hat-section von Mises stress contour at (a) Upon impact; (b) $d_z = 4.85$ mm; (c) d_z=6.85 mm. The impactor is hidden for clarity. The present ICME framework is capable of visualizing structural level responses and the microstructure responses. In this case, only those elements mentioned in Fig. 21 are visualized.

hard to capture experimentally, for the cause of failure at the structural level. New microstructure can be then designed to sustain the loading and improve the overall structural performance.

6. Conclusion

The present work introduced a predictive and efficient ICME multiscale modeling framework for UD CFRP materials. The main workflow of the framework is explained in detail, and experimental validations are provided. The predictive framework links UD CFRP microstructures to structural level models for accurate prediction of the structural performance. Two sample cases studies, the UD off-axial tensile test and the UD hat-section dynamic three-point bending test, are presented using the proposed ICME modeling framework. The predicted performance indices are validated against experimental data confirming a good agreement. Microstructure evolution in the UD structure is captured by UD CFRP RVEs, which reveal microstructural evolution, including stress contour and matrix damage. The ICME framework is general and can be applied to other Fiber Reinforced Polymer (FRP) systems, such as glass fiber reinforced polymer, for structure performance prediction. Along with the microstructure information, the work presented in this paper should provide guidance to existing experimental based composites design workflows to accelerate the design process.

Future work of the present multiscale modeling framework for UD CFRP includes: (1) Incorporation of the interphase in the UD RVE for fiber-matrix debonding; (2) Consideration of microstructure uncertainties, such as fiber misalignment and fiber volume fraction, for quantitative measurement of the microstructure effect. (3) Extension to other composite material systems.

Declaration of competing interest

The authors declare that they have no known competing financial interests or personal relationships that could have appeared to influence the work reported in this paper.

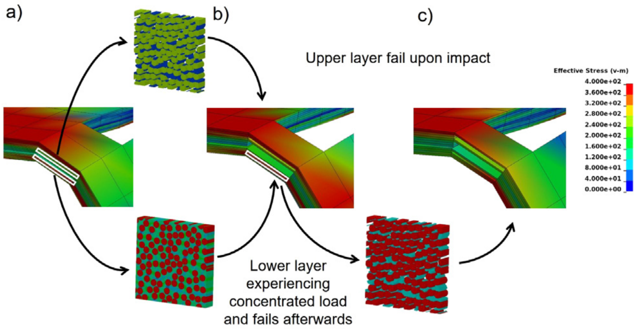

Fig. 23. Magnified view of the hat-section with UD CFRP microstructure evolution at (a) d_z=5.91 mm; (b) d_z=6.13 mm; (c) d_z=6.78 mm. The UD microstructure damage processes in two marked elements are visualized.

Acknowledgments

The financial support for this project was provided by the U.S. Department of Energy's Office of Energy Efficiency and Renewable Energy (EERE), under Award Number DE-EE0006867. W.K.L acknowledges the support of the National Science Foundation, United States under Grant No. MOMS/CMMI-1762035.

Appendix A. Self-consistent clustering analysis — solution procedure

The present formulation is based on the evaluation of DNS solution of a high fidelity voxel mesh using Fast Fourier Transformation (FFT) method, initially proposed by Moulinec et al. The discretized form of Lippmann–Schwinger equation, originally used to solve for local responses in the FFT method, is presented. Offline and online stages of SCA are then presented, completing the fast DNS evaluation part of the concurrent framework for UD CFRP.

The DNS of RVE can be conveniently solved by FFT based homogenization approach, where the local strain of each voxel is computed by

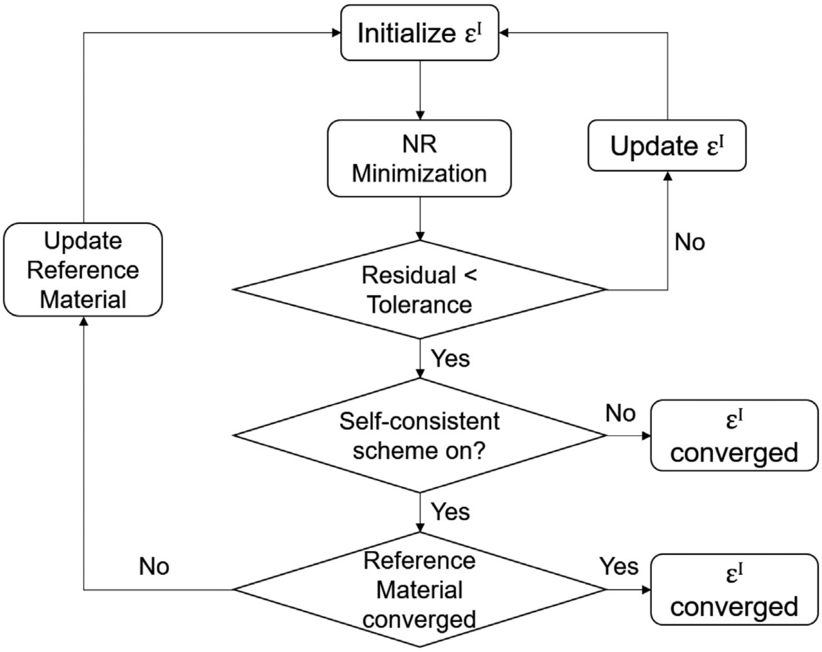

Fig. A.1. SCA flow chart for the solving the Lippmann–Schwinger equation.

resolving Eq. (A.1)

$$\boldsymbol{\varepsilon}(\boldsymbol{x}) = \boldsymbol{\varepsilon}^M - \boldsymbol{\Gamma}^{\mathbf{0}}(\boldsymbol{x}) * (\boldsymbol{\sigma}(\boldsymbol{x}) - \boldsymbol{C}^0 : \boldsymbol{\varepsilon}(\boldsymbol{x})) \tag{A.1}$$

By re-writting the convolution term and stress and strain in incremental form, we have Eq. (A.2) as shown:

$$\Delta\boldsymbol{\varepsilon}(\boldsymbol{x}) = \Delta\boldsymbol{\varepsilon}^M - \int_\Omega \boldsymbol{\Gamma}^{\mathbf{0}}(\boldsymbol{x},\boldsymbol{x}') : (\Delta\boldsymbol{\sigma}(\boldsymbol{x}') - \boldsymbol{C}^0 : \Delta\boldsymbol{\varepsilon}(\boldsymbol{x}'))d\boldsymbol{x}' \tag{A.2}$$

where $\Delta\boldsymbol{\varepsilon}(\boldsymbol{x})$ is the local strain increment and $\Delta\boldsymbol{\varepsilon}^M$ is the applied macroscopic strain increment upon the RVE. $\boldsymbol{C}^0$ is the reference material and $\Delta\boldsymbol{\sigma}(\boldsymbol{x}')$ and $\Delta\boldsymbol{\varepsilon}(\boldsymbol{x}')$ are the stress and strain increments in the reference domain. $\boldsymbol{\Gamma}^0$ is the isotropic Green's function based on reference material $\boldsymbol{C}^0$.

SCA utilizes an incremental form of the discretized Lippmann–Schwinger Equation that greatly reduces the total number of degrees of freedom of the RVE. The idea is to assume that in a RVE composed of N voxel elements and that those that behave the same in elastic region will always behave similarly. Provided that N voxel elements can be grouped into K clusters, the original RVE domain Ω is decomposed into $\Omega^1, \Omega^2, \ldots, \Omega^K$. Here, it is important to introduce a characteristic function that converts the cluster-wise average in Ω^I to the whole domain Ω, as shown in Eq. (A.3):

$$\frac{1}{|\Omega|^I}\int_{\Omega^i}[QOI]d\boldsymbol{x} = \frac{1}{c^I|\Omega|}\int_\Omega \chi^I(\boldsymbol{x})[QOI]d\boldsymbol{x},\ \chi^I(\boldsymbol{x}) = \begin{cases} 1, if\ \boldsymbol{x}\in\Omega^I \\ 0, otherwise \end{cases} \tag{A.3}$$

where $|\Omega|^I$ is the domain volume of cluster i, c^I is the volume fraction of cluster i in the whole domain, and $|\Omega|$ is the whole domain volume. Now it is possible to formulate the discretized form of incremental Lippmann–Schwinger equation, which is given in Eq. (A.4) below for each cluster.

$$\frac{1}{c^I|\Omega|}\int_\Omega \chi^I(\boldsymbol{x})\Delta\boldsymbol{\varepsilon}(\boldsymbol{x})d\boldsymbol{x} = \Delta\boldsymbol{\varepsilon}^M - \frac{1}{c^I|\Omega|}\int_\Omega\int_\Omega \chi^I(\boldsymbol{x})\boldsymbol{\Gamma}^{\mathbf{0}}(\boldsymbol{x},\boldsymbol{x}') : (\Delta\boldsymbol{\sigma}(\boldsymbol{x}') - \boldsymbol{C}^0 : \Delta\boldsymbol{\varepsilon}(\boldsymbol{x}'))d\boldsymbol{x}'d\boldsymbol{x} \tag{A.4}$$

Due to the definition of χ function, it is possible to have following relationship for $\boldsymbol{\sigma}(\boldsymbol{x}')$ and $\boldsymbol{\epsilon}(\boldsymbol{x}')$ in Eq. (A.5)

$$\Delta\boldsymbol{\sigma}(\boldsymbol{x}') = \sum_{J=1}^K \chi^J(\boldsymbol{x}')\Delta\boldsymbol{\sigma}^J, \quad \Delta\boldsymbol{\varepsilon}(\boldsymbol{x}') = \sum_{J=1}^K \chi^J(\boldsymbol{x}')\Delta\boldsymbol{\varepsilon}^J \tag{A.5}$$

Now, it is possible to plug in Eq. (A.5) into Eq. (A.4) to have final form of discretized Lippmann–Schwinger equation, as shown in Eq. (A.6):

$$\Delta\boldsymbol{\varepsilon}^I = \Delta\boldsymbol{\varepsilon}^M - \sum_{J=1}^K \left[\frac{1}{c^I|\Omega|}\int_\Omega\int_\Omega \chi^I(\boldsymbol{x})\chi^J(\boldsymbol{x}')\boldsymbol{\Gamma}^{\mathbf{0}}(\boldsymbol{x},\boldsymbol{x}')d\boldsymbol{x}'d\boldsymbol{x} : (\Delta\boldsymbol{\sigma}^J - \boldsymbol{C}^0 : \Delta\boldsymbol{\varepsilon}^J)\right] \tag{A.6}$$

Note that in Eq. (A.6), the polarization stress is separated out from the convolution part of the Lippmann–Schwinger equation. This allows one to define an interaction tensor D^{IJ} as shown in Eq. (A.7):

$$\boldsymbol{D}^{IJ} = \frac{1}{c^I|\Omega|}\int_\Omega\int_\Omega \chi^I(\boldsymbol{x})\chi^J(\boldsymbol{x}')\boldsymbol{\Gamma}^{\mathbf{0}}(\boldsymbol{x},\boldsymbol{x}')d\boldsymbol{x}'d\boldsymbol{x} \tag{A.7}$$

So Eq. (A.6) is simplified as Eq. (A.8):

$$\Delta\boldsymbol{\varepsilon}^I = \Delta\boldsymbol{\varepsilon}^M - \sum_{J=1}^K \left[\boldsymbol{D}^{IJ} : (\Delta\boldsymbol{\sigma}^J - \boldsymbol{C}^0 : \Delta\boldsymbol{\varepsilon}^J)\right] \tag{A.8}$$

For any given RVE with N voxel elements, it is necessary to first decompose the whole domain into K clusters so one can actually use Eq. (A.4) to perform reduced order modeling of an RVE. Therefore, as mentioned, SCA is a two-stage homogenization method: Stage 1. Offline system reduced order modeling, including domain decomposition and calculation of interaction tensor D_{IJ} between all cluster pairs; Stage 2. online prediction of elasto-plastic material responses of the RVE. Details of each stage is provided as below.

The solution procedure of the online stage requires minimization of the residual, given in Eq. (A.9):

$$\boldsymbol{r}^I = -\Delta\boldsymbol{\varepsilon}^M + \Delta\boldsymbol{\varepsilon}^I + \sum_{J=1}^K \left[\boldsymbol{D}^{IJ} : (\Delta\boldsymbol{\sigma}^J - \boldsymbol{C}^0 : \Delta\boldsymbol{\varepsilon}^J)\right],\ I = 1,2,3,\ldots,K \tag{A.9}$$

Newton–Raphson (NR) method is applied to find strain increment $\Delta\boldsymbol{\varepsilon}^J$ at each loading step. Linearizing Eq. (A.10) with respect to $\Delta\boldsymbol{\varepsilon}^J$ gives:

$$\boldsymbol{r}^I + \frac{\partial \boldsymbol{r}^I}{\partial\Delta\boldsymbol{\varepsilon}^J}\delta\boldsymbol{\varepsilon}^I = 0,\ \ I = 1,2,3,\ldots,K \tag{A.10}$$

where the Jacobian $\frac{\partial r^I}{\partial \Delta\epsilon^J}$, denoted as $\boldsymbol{M}^{IJ}$, is given in Eq. (A.11):

$$\boldsymbol{M}^{IJ} = \delta_{IJ}\boldsymbol{I} + \sum_{J=1}^{K} \boldsymbol{D}^{IJ} : \left[\boldsymbol{C}^{J}_{alg} - \boldsymbol{C}^{0}\right], \quad I = J = 1, 2, 3, \dots, K \tag{A.11}$$

Note here the reference material needs to be as close to the effective macroscopic tangent modulus C^{eff} of the RVE as possible. This would require one to update C^0 based on C^{eff} when the residual is minimized. Here, the self-consistent scheme for updating the reference material C^0 can be found in [17,35].

A algorithm flow chart for SCA online stage is provided in Fig. A.1 for readers' reference.

Appendix B. Supplementary data

Supplementary material related to this article can be found online at https://doi.org/10.1016/j.compscitech.2019.107922.

References

[1] Gregory B. Olson, Designing a new material world, Science 288 (5468) (2000) 993–998.

[2] Su Hao, Wing Kam Liu, Brian Moran, Franck Vernerey, Gregory B. Olson, Multi-scale constitutive model and computational framework for the design of ultra-high strength, high toughness steels, Comput. Methods Appl. Mech. Engrg. 193 (17–20) (2004) 1865–1908.

[3] Hui Cheng, Jiaying Gao, Orion Landauer Kafka, Kaifu Zhang, Bin Luo, Wing Kam Liu, A micro-scale cutting model for UD CFRP composites with thermo-mechanical coupling, Compos. Sci. Technol. 153 (2017) 18–31.

[4] Ying Li, Brendan C. Abberton, Maartin Kröger, Wing Kam Liu, Challenges in multiscale modeling of polymer dynamics, in: Polymers, vol. 5, 2013, pp. 751–832, http://dx.doi.org/10.3390/polym5020751.

[5] Wing Kam Liu, Cahal McVeigh, Predictive multiscale theory for design of heterogeneous materials, Comput. Mech. 42 (2) (2008) 147–170, http://dx.doi.org/10.1007/s00466-007-0176-8.

[6] Wing Kam Liu, Dong Qian, Stefano Gonella, Shaofan Li, Wei Chen, Shardool Chirputkar, Multiscale methods for mechanical science of complex materials: Bridging from quantum to stochastic multiresolution continuum, Internat. J. Numer. Methods Engrg. 83 (8–9) (2010) 1039–1080.

[7] Ted Belytschko, Wing Kam Liu, Brian Moran, Khalil Elkhodary, Nonlinear Finite Elements for Continua and Structures, John wiley & sons, 2013.

[8] Guohe Li, Jiaying Gao, Orion L. Kafka, Jacob Smith, Wing Kam, Implementation and application of the multiresolution continuum theory, Comput. Mech. 63 (4) (2019) 631–647, http://dx.doi.org/10.1007/s00466-018-1613-6.

[9] Cahal McVeigh, Franck Vernerey, Wing Kam Liu, L. Cate Brinson, Multiresolution analysis for material design, Comput. Methods Appl. Mech. Engrg. 195 (37–40) (2006) 5053–5076, http://dx.doi.org/10.1016/j.cma.2005.07.027.

[10] M.G.D. Geers, V.G. Kouznetsova, W.A.M. Brekelmans, Multi-scale computational homogenization: Trends and challenges, J. Comput. Appl. Math. 234 (7) (2010) 2175–2182, http://dx.doi.org/10.1016/j.cam.2009.08.077.

[11] George J. Dvorak, Transformation field analysis of inelastic composite materials, Proc. R. Soc. Lond. Ser. A Math. Phys. Eng. Sci. 437 (1900) (1992) 311–327.

[12] J.C. Michel, P. Suquet, Computational analysis of nonlinear composite structures using the nonuniform transformation field analysis, Comput. Methods Appl. Mech. Engrg. 193 (48–51) (2004) 5477–5502, http://dx.doi.org/10.1016/j.cma.2003.12.071.

[13] S. Roussette, J.C. Michel, P. Suquet, Nonuniform transformation field analysis of elastic-viscoplastic composites, Compos. Sci. Technol. 69 (1) (2009) 22–27, http://dx.doi.org/10.1016/j.compscitech.2007.10.032.

[14] David Amsallem, Charbel Farhat, Interpolation method for adapting reduced-order models and application to aeroelasticity, AIAA J. 46 (7) (2008) 1803–1813.

[15] Kevin Carlberg, Charbel Bou-Mosleh, Charbel Farhat, Efficient non-linear model reduction via a least-squares Petrov–Galerkin projection and compressive tensor approximations, Internat. J. Numer. Methods Engrg. 86 (2) (2011) 155–181.

[16] Zeliang Liu, M.A. Bessa, Wing Kam Liu, Self-consistent clustering analysis: An efficient multi-scale scheme for inelastic heterogeneous materials, Comput. Methods Appl. Mech. Engrg. 306 (2016) 319–341, http://dx.doi.org/10.1016/j.cma.2016.04.004, http://dx.doi.org/10.1016/j.cma.2016.04.004.

[17] Zeliang Liu, Mark Fleming, Wing Kam, Microstructural material database for self-consistent clustering analysis of elastoplastic strain softening materials, Comput. Methods Appl. Mech. Engrg. 330 (2018) 547–577, http://dx.doi.org/10.1016/j.cma.2017.11.005.

[18] Zhaoxu Meng, Miguel A. Bessa, Wenjie Xia, Wing Kam Liu, Sinan Keten, Predicting the macroscopic fracture energy of epoxy resins from atomistic molecular simulations, Macromolecules 49 (24) (2016) 9474–9483.

[19] Xiaoming Bai, Miguel A. Bessa, António R. Melro, Pedro P. Camanho, Licheng Guo, Wing K. Liu, High-fidelity micro-scale modeling of the thermo-visco-plastic behavior of carbon fiber polymer matrix composites, Compos. Struct. 134 (2015) 132–141.

[20] A.R. Melro, P.P. Camanho, F.M. Andrade Pires, S.T. Pinho, Micromechanical analysis of polymer composites reinforced by unidirectional fibres: Part I–Constitutive modelling, Int. J. Solids Struct. 50 (11–12) (2013) 1897–1905.

[21] Ramin Bostanabad, Biao Liang, Jiaying Gao, Wing Kam Liu, Jian Cao, Danielle Zeng, Xuming Su, Hongyi Xu, Yang Li, Wei Chen, Uncertainty quantification in multiscale simulation of woven fiber composites, Comput. Methods Appl. Mech. Engrg. 338 (2018) 506–532, http://dx.doi.org/10.1016/j.cma.2018.04.024.

[22] Jiaying Gao, Biao Liang, Weizhao Zhang, Zeliang Liu, Puikei Cheng, Ramin Bostanabad, Jian Cao, Wei Chen, Wing Kam Liu, Xuming Su, Danielle Zeng, John Zhao, Multiscale Modeling of Carbon Fiber Reinforced Polymer (CFRP) for Integrated Computational Materials Engineering Process, Ford Motor Company, 2017, http://dx.doi.org/10.12783/asc2017/15188.

[23] Weizhao Zhang, Huaqing Ren, Zequn Wang, Wing K. Liu, Wei Chen, Danielle Zeng, Xuming Su, Jian Cao, An Integrated Computational Materials Engineering Method for Woven Carbon Fiber Composites Preforming Process, vol. 1769, 2016, http://dx.doi.org/10.1063/1.4963592.

[24] Qingping Sun, Haiding Guo, Guowei Zhou, Zhaoxu Meng, Zhangxing Chen, Hongtae Kang, Sinan Keten, Xuming Su, Experimental and computational analysis of failure mechanisms in unidirectional Carbon fiber reinforced polymer laminates under longitudinal compression loading, Compos. Struct. 203 (2018) 335–348.

[25] Qingping Sun, Zhaoxu Meng, Guowei Zhou, Shih-Po Lin, Hongtae Kang, Sinan Keten, Haiding Guo, Xuming Su, Multi-scale computational analysis of unidirectional carbon fiber reinforced polymer composites under various loading conditions, Compos. Struct. 196 (2018) 30–43.

[26] Canio Hoffarth, Joseph Harrington, Subramaniam D. Rajan, Robert K. Goldberg, Kelly S. Carney, Paul DuBois, Gunther Blankenhorn, Verification and validation of a three-dimensional generalized composite material model, 2015.

[27] S. Chand, Review carbon fibers for composites, J. Mater. Sci. 35 (6) (2000) 1303–1313.

[28] Tadashi Ohsawa, Minoru Miwa, Masato Kawade, Eiki Tsushima, Axial compressive strength of carbon fiber, J. Appl. Polym. Sci. 39 (8) (1990) 1733–1743.

[29] Louise A. Powell, William E. Luecke, Matthias Merzkirch, Katherine Avery, Tim Foecke, High strain rate mechanical characterization of Carbon fiber reinforced polymer composites using digital image correlations, SAE Int. J. Mater. Manf. 10 (2017) 138–146, http://dx.doi.org/10.4271/2017-01-0230.

[30] Matthias Merzkirch, Louise Ahure Powell, Tim Foecke, Measurements of Mode I Interlaminar Properties of Carbon Fiber Reinforced Polymers Using Digital Image Correlation, in: Key Engineering Materials, vol. 742, Trans Tech Publ, 2017, pp. 652–659.

[31] Elizabeth M.C. Jones, Mark A. Iadicola, A Good Practices Guide for Digital Image Correlation, International Digital Image Correlation Society, 2018.

[32] M. Merzkirch, Mechanical Characterization Using Digital Image Correlation - Advanced Fibrous Composite Laminates, Springer Nature Switzerland AG, to be submitted in 2020.

[33] L.T. Harper, C. Qian, T.A. Turner, S. Li, N.A. Warrior, Representative volume elements for discontinuous carbon fibre composites–part 2: Determining the critical size, Compos. Sci. Technol. 72 (2) (2012) 204–210.

[34] Guowei Zhou, Qingping Sun, Danielle Zeng, Dayong Li, Xuming Su, Experiment and simulation study on unidirectional Carbon fiber composite component under dynamic 3 point bending loading, SAE Int. J. Mater. Manuf. 11 (2018).

[35] Cheng Yu, Orion L. Kafka, Wing Kam Liu, Self-consistent clustering analysis for multiscale modeling at finite strains, Comput. Methods Appl. Mech. Engrg. 349 (2019) 339–359.